Materials and Methods:

Optical design. Optics were designed around a Zeiss Axiovert S100TV microscope body. The sample is excited using a supercontinuum laser source with internal pulse picker to halve the repetition rate to 39 MHz (NKT SuperK EXW-12). The laser is first filtered with a colored glass filter to remove infrared (Thorlabs FGS900), and a FITC filter set is used for imaging (Semrock: excitation FF02-475/50, dichroic FF506-Di03, and emission FF01-540/50). The sample is imaged in epifluorescence mode using an Olympus 20X/0.95 NA XLUMPlanFl water immersion objective and excited with 1.5 mW total power ($\sim$5 W/cm^2 intensity at the sample). Images are acquired at 1 kHz frame rate using a Hamamatsu ORCA-Quest camera operating in standard readout mode with 0.44 electron/pixel read noise.

A first pair of relay lenses after the output port of the microscope creates an image plane near the Pockels cell crystals, and a second pair of lenses is used to relay this image onto the camera sensor. The Pockels cell is placed between polarizing beamsplitter cubes (Thorlabs PBS251) along with a liquid crystal variable waveplate that is used to zero static birefringent phase shift (Thorlabs LCC1421-A). In order to ensure equal optical path lengths and to allow independent focusing of the two output images, a third polarizing beamsplitter cube is used to combine the separated paths before the final relay lens as shown in Fig. 1(A). By placing an image plane near the Pockels cell crystals, it is easier to align the crystals such that optimal performance is obtained in the presence of thermal stress.

Pockels cell and RF system. A custom lithium tantalate Pockels cell was developed with Leysop Inc. A pair of crystals (9x9x10 mm each) is used with electric field applied transverse to the optical axis (Fig. S1). The crystals are rotated 90 degrees relative to each other in a standard configuration that also enables cancellation of off-axis birefringent phase shifts and proves optimal for wide-field imaging (compared to common DKDP crystals which have limited angular acceptance (*14*)). Lithium tantalate is also a good choice for imaging applications due to its low birefringence. Dielectric losses dissipate power within the crystals, so they are cooled by thermally conductive aluminum nitride ceramic plates connected to a water cooling circuit.

For an applied voltage V, the Pockels cell produces a birefringent phase shift $\delta = 2\pi(n_e^3 r_{33} - n_o^3 r_{13})VL/d\lambda$ where n_o and n_e are the ordinary and extraordinary refractive indices, r_{33} and r_{13} are the electro-optic coefficients, L is the crystal length, and d is the aperture. The voltage corresponding to a π phase shift (V_π) for the Pockels cell used here is approximately 1.2 kV (Fig. S3). The time-dependent birefringent phase shift results in an intensity modulation through crossed polarizers given by $g(t) = \sin^2(\delta(t)/2)$ and $u(t) = \cos^2(\delta(t)/2)$ for the gated (G) and ungated (U) channels respectively. For resonant drive, this results in a gating function of the form $g(t) = \sin^2[A\pi \sin(\omega t)/2]$ where A is the drive strength in units of V_π. Note that positive and negative voltage across the Pockels cell result in the same transmission, so that the optical gating waveform has twice the frequency of the drive voltage.

The Pockels cell and its resonant circuit are housed in a grounded aluminum enclosure, shown in Fig. S2. The Pockels cell acts as a capacitive load in a resonant transformer. The primary is a half turn copper strap, and the secondary comprises 11 turns of 3/16" copper tubing electrically in series with the Pockels cell electrodes (Fig. S3). This transformer achieves $\sim V_\pi$ at 19.5 MHz using 9.3 W RF power and presents an impedance-matched 50 Ω load to the drive electronics. Fine tuning of the resonant frequency is accomplished by monitoring S11 on a network analyzer (HP 4395A/87511A or NanoVNA) and adjusting a 10 pF trimmer capacitor (Sprague-Goodman SGNMNC1103) using a stepper motor. Drive is provided by a class-A amplifier (ENI 325LA) with transmitted and reflected power monitored on a SWR meter (Youmei RS-70). The RF signal originates from the laser and is used as input to a direct digital synthesizer (Novatech 409B-AC) that produces a phase locked 19.5 MHz drive with a computer controlled phase offset. This system has proven highly stable, and it allows for continuous modulation without phase drift.

Sample preparation. To express the pAce indicator in MBON-γ1pedc> α/β neurons, we crossed the MB085C-GAL4 flies with 20×UAS-pAce flies and collected their progenies for imaging experiments. To create an imaging window in the fly cuticle, we mounted flies onto a customized holder and used a laser microsurgery system based on a 193 nm wavelength excimer laser (GamLaser; EX5 ArF), as detailed in our prior work (*17*, *18*). In each fly, the laser microsurgery created a 150 μm

diameter hole (30–40 laser pulses, delivered at 100 Hz, 36 μJ per pulse as measured at the specimen plane). Immediately after surgery, we applied 1 μL of UV epoxy (NOA 68, Norland; Refractive index: 1.54; Transmission 420–1000 nm: $\sim 100\%$) and cured it for 30 s to seal the cuticle opening. Then, we glued a coverslip (22 $\times$ 22 mm, No. 0, Electron Microscope Sciences) above the fly's head to be compatible with water immersion imaging.

Mechanical stimulation. We used two methods to apply mechanical stimulation to the fly. In the first method a 5 inch speaker was placed 6 cm above the sample plane and driven to produce 85-90 dBA at the sample. This was effective at vibrating the sample stage near resonance frequencies without much in-plane motion, and resulted in observed phase locking such as shown in Figs. 2 and S10(A). For the second method, to provide a direct and tunable in-plane shaking stimulus, we used a small piezoelectric stage (Physik Instrumente P-915K238) driven with a function generator. This allowed stimulus frequency sweeps in Figs. 4 and S10(B).

Analysis. The gated (G) and ungated (U) image pixels are registered using an affine transformation that is determined from a bright-field image of a grid micrometer slide (Electron Microscopy Sciences slide S29). In order to measure the gating functions $g(t)$ and $u(t)$ which serve as the instrument response function (IRF), a quenched fluorescein standard is used. This standard is prepared using 170 μL saturated fluorescein solution added to 1 mL of saturated potassium iodide solution which has been brought to pH 10 with potassium hydroxide. The G and U intensities measured on the camera are determined by the convolution of the IRF with the unknown lifetime $I(t,\tau)$. For a particular Pockels cell drive phase ϕ, $G(\phi,\tau) = \int I(t,\tau)g(t-\phi/\omega)\mathrm{d}t$ and $U(\phi_0,\tau) = \int I(t,\tau)u(t-\phi/\omega)\mathrm{d}t$, where the gating functions are normalized such that $g(t)+u(t) = 1$. These convolutions were directly measured by varying the Pockels cell phase ϕ relative to the laser (*13*). The resulting intensity curve (Figs. 1(B) and S1(D)) may be fit to determine the lifetime by sampling at multiple phase points. Alternatively, a single optimal phase ϕ may be chosen where intensity ratios can be used to estimate lifetime. For the selected phase, a lookup table is calculated by numerically convolving the experimentally measured IRF with single exponential decays.

This table allows conversion between measured intensity ratio G/U and a lifetime estimate (Fig. S2(B-D)). Noise limits are fundamentally determined by shot noise in the G and U images, and the achievable lifetime estimation sensitivity is plotted in Fig. S2(B). When generating lifetime traces, the G/U intensity ratio, IRF, and resulting lifetime lookup table are all determined locally from the same image region of interest.

To generate lifetime movies, lifetime images are determined from pixel intensity ratios and overlayed with a transparency mask generated from the intensity image to show sample structure. Motion correction is first applied using piecewise affine transformations that are determined every 20 frames. For spike-triggered averaging, spikes locations are identified using a highpass filtered trace, then images corresponding to a time window before and after each spike are combined into a single movie that is temporally averaged over $\sim$ 300 spikes referenced to the peak. Triggered movies are interpolated by generating 20 time points per millisecond through linear interpolation of each pixel trace. Due to the rolling shutter readout of the sCMOS camera, there is a small time delay between readout of different sensor regions that depends on the pixel row number. This rolling shutter delay is corrected by applying a shift to the interpolated pixel time traces using the known row readout time of the camera sensor. For non-averaged movies of sub-threshold signals, a moving average of ten frames is used to reveal slower spatial dynamics. A moving average image calculated from 1000 frames is also subtracted to remove long-term drifts. Gaussian filtering is applied to the lifetime movies to average over spatial noise. Average spike waveforms displayed in Figs. 1(F,G), 2(G,H), S5 and S6 correspond to the average spike calculated across indicated image ROIs. Here 20 points per millisecond are interpolated, and rolling shutter corrections are applied using the average row value for each ROI. In Figs. 1 and 2, piecewise cubic interpolation is used. In Figs. S5 and S6, spline interpolation is used and spike timing is determined from the peak. For comparing recordings in the different neuron sub-regions, a three frame moving average is applied.

In Fig. 2, signal-to-noise ratio (SNR) is determined by comparing spike amplitude to the RMS noise of the fluorescence baseline. Spike amplitude is determined by subtracting a 20 Hz low-pass filtered waveform from the activity traces. The RMS noise floor is determined by first replacing each spike in an interval of ± 3 points on each side of the spike time with the moving average. The

resulting trace is then highpass filtered at 50 Hz and the standard deviation corresponds to the RMS noise value. The RMS noise distribution is shown in Fig. 1(C) for an example trace and is also used to calculate the lifetime sensitivity. Lifetime sensitivity and responsivity values are calculated using all seven neurons shown in Figs. 1 and 2. The power spectral density (PSD) is determined using Welch's method applied to the spike-removed traces described above. Because responsivities $\Delta F/F$ and $\Delta\tau/\tau$ are not equal, the lifetime traces and shot noise limits are normalized by a correction factor determined by comparing intensity and lifetime spike amplitudes. Otherwise the lifetime trace would have an artificially reduced noise level and direct comparison of power spectra would not be possible. The spike detection fidelity d' is calculated from the raw data traces using a data interval of 12 ms on each side of the spike time (*20*, *21*). To analyze phase locking in Fig. 2(K,L), a bandpass filtered trace (5 Hz bandwidth, infinite impulse response), is used to derive a phase reference by applying a Hilbert transform. Each spike location on the original trace is then assigned a phase value using the reference. The length of the average phase vector $\sum_i \cos(\theta_i)/N_{\mathrm{AP}}$ vs. frequency is plotted by scanning the bandpass center frequency.

Spectrograms are determined using Welch's method. In Fig. 4(C), phase locked activity is observed in the spectrogram as increased power at the stimulus frequency during spike activity bursts. By plotting the autocorrelation in Fig. 4(D) along the y-axis as a function of time (150 ms window length), it is possible to visualize the phase synchronization of spikes to the mechanical cross-talk, which is visible as a diagonal line at the stimulus frequency in the spectrogram. Phase locking is seen at either the fundamental or half-harmonic stimulus frequencies here (i.e. spiking every cycle or every other cycle). We also note that the start and stop of mechanical cross-talk signal tends to coincide with a spike burst as shown in Fig. S10(B).

No data exclusion criteria were preestablished. Sample sizes were determined from the standards of the voltage imaging field. Experimental results were biologically replicated across multiple flies (>30) and days of imaging. Further, technical replication was performed at each image frame throughout the recordings.

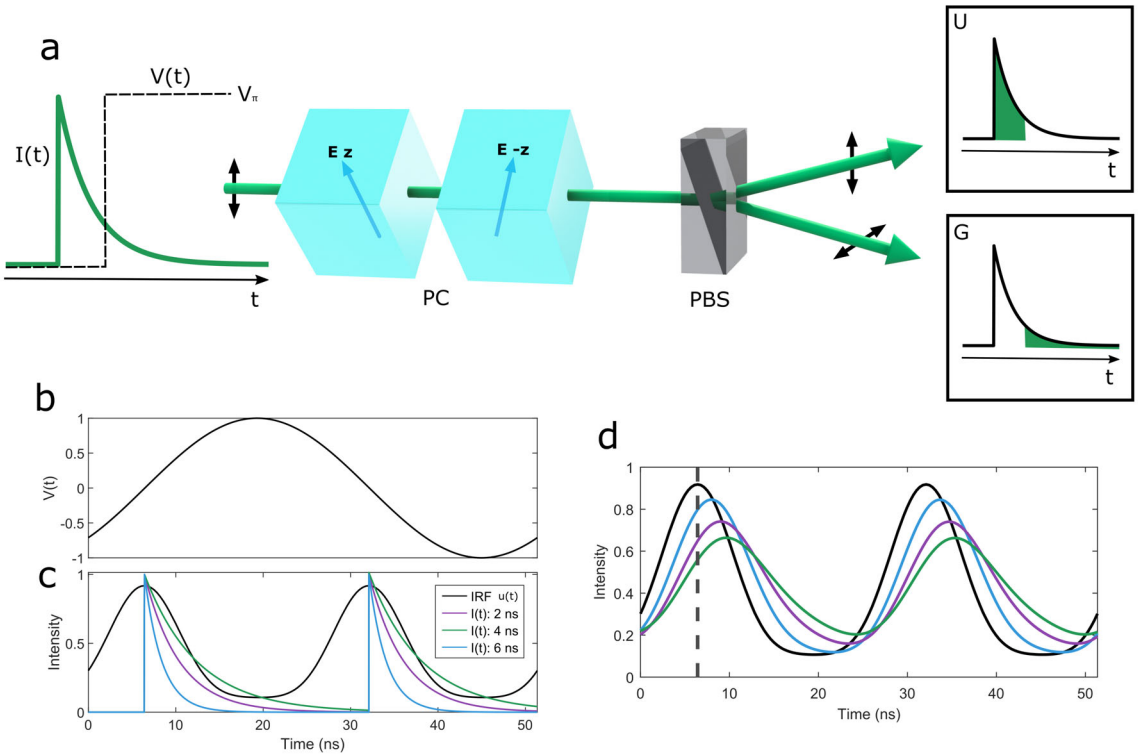

Fig. S1: EO-FLIM method. **(A)** Schematic diagram of EO-FLIM gating. A fluorescence decay at left is gated by an ideal voltage step function applied to the Pockels cell (PC) at a time delay after the excitation pulse. Light arriving before the voltage step is captured in ungated output image (U) after the polarizing beamsplitter (PBS). Light arriving after the voltage step has its polarization rotated by 90 degrees and is captured in gated output image (G). All light from the original decay is preserved up to optical losses. To optimize imaging performance, a transverse field lithium tantalate Pockels cell is employed with electric field applied perpendicular to the optical axis. In order to compensate for static and off-axis birefringence, a pair of crystals is used with a 90 degree relative rotation (crysal Z axis indicated) and reversed electric field directions. **(B)** Instead of an ideal step-function, our experiments applied a sinusoidal voltage drive to the crystal with ∼1.2 kV amplitude. **(C)** Experimentally realized gating function u(t) in the ungated channel is plotted along with simulated 2, 4, and 6 ns fluorescence decays, I(t). This relative phase setting is used for all acquired data. **(D)** Plot of output intensity U as a function of phase delay between excitation laser pulses and u(t). This represents the convolution of I(t) with u(t). Simulated phase traces are plotted for the three lifetimes in (C). For fast voltage imaging, a single phase point from this trace is sampled, corresponding to one camera exposure (vertical line) where lifetime is estimated from the ratio of G and U image intensities. Note that $u(t) + g(t) = 1$, so g(t) is not shown here.

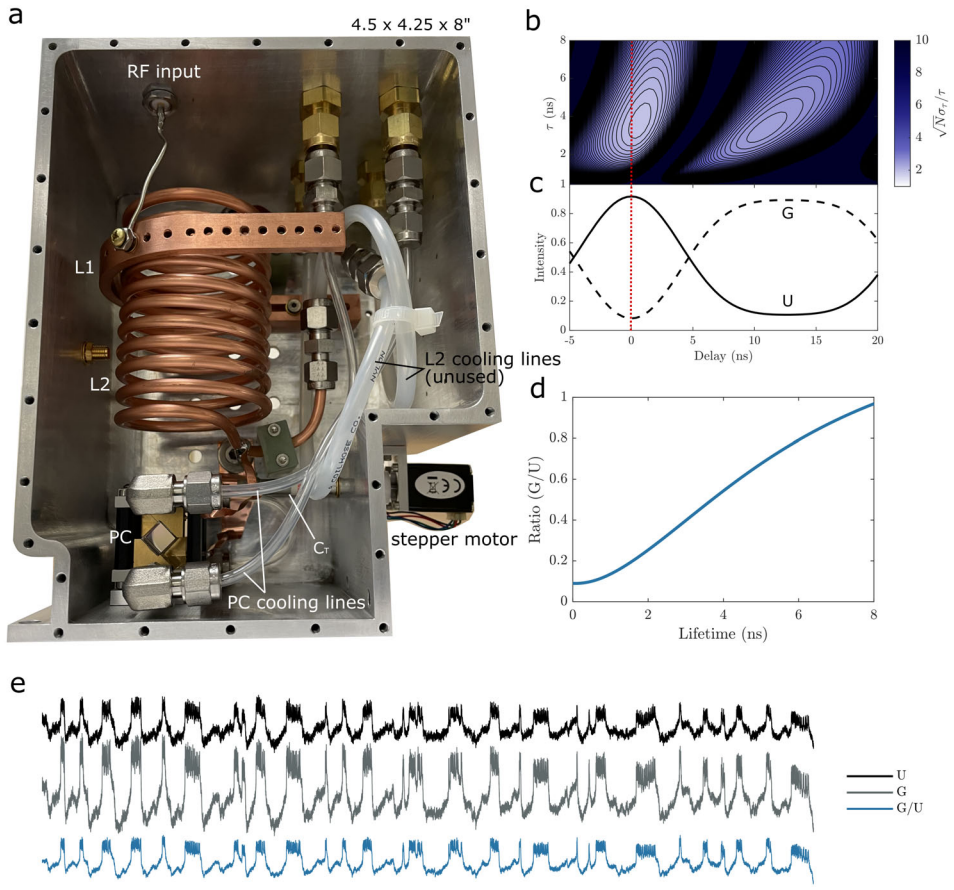

Fig. S2: Resonant Pockels cell gating. (**A**) Pockels cell (PC - aperture at bottom left) and radio frequency (RF) drive circuit inside grounded enclosure. A resonant transformer is used to present a high-voltage drive to the Pockels cell using 9.3 W of input RF power. The transformer is tuned to provide a 50 ohm load to the driving electronics. The primary L1 is a half turn copper strap, and the secondary L2 consists of a 11 turn coil of copper tubing connected in series with the Pockels cell, which acts as a capacitor. A trim capacitor C_T is adjusted by a stepper motor to tune the circuit's resonance frequency. Water cooling is provided to the PC, and additional lines for oil cooling of L2 were included but not used during normal operation. The entire assembly is mounted on a tilt and rotation platform for alignment (Newport model 36). (**B**) Photon normalized estimation accuracy (F number or $\sqrt{N}\sigma_\tau/\tau$) for EO-FLIM is plotted as a function of lifetime and phase delay using the experimental instrument response function plotted in (C). F=1 corresponds to the fundamental limit for an optimal lifetime measurement. (**C**) Instrument response function measured with quenched fluorescein dye. The gated (G) and ungated (U) image intensities are normalized and plotted as a function of phase delay as in Fig. S1. (**D**) Lookup table used for converting a measured intensity ratio G/U to a fluorescence lifetime value. In the absence of experimental noise, lifetime error is determined by photon shot noise in the G and U channels and the slope of the lookup table function. (**E**) Example voltage imaging traces for gated (G), ungated (U), and ratio (R) channels are plotted on the same vertical scale normalized to their mean values. The direct G and U traces show that despite 80% of intensity being captured in U, the G channel has enhanced spike height and voltage responsivity. This happens because a positive intensity change also results in a positive lifetime change, which transfers intensity from U into G. The ratio signal shows attenuated overall response but improved SNR. It is directly proportional to lifetime for small changes since the lookup table in (D) is locally linear.

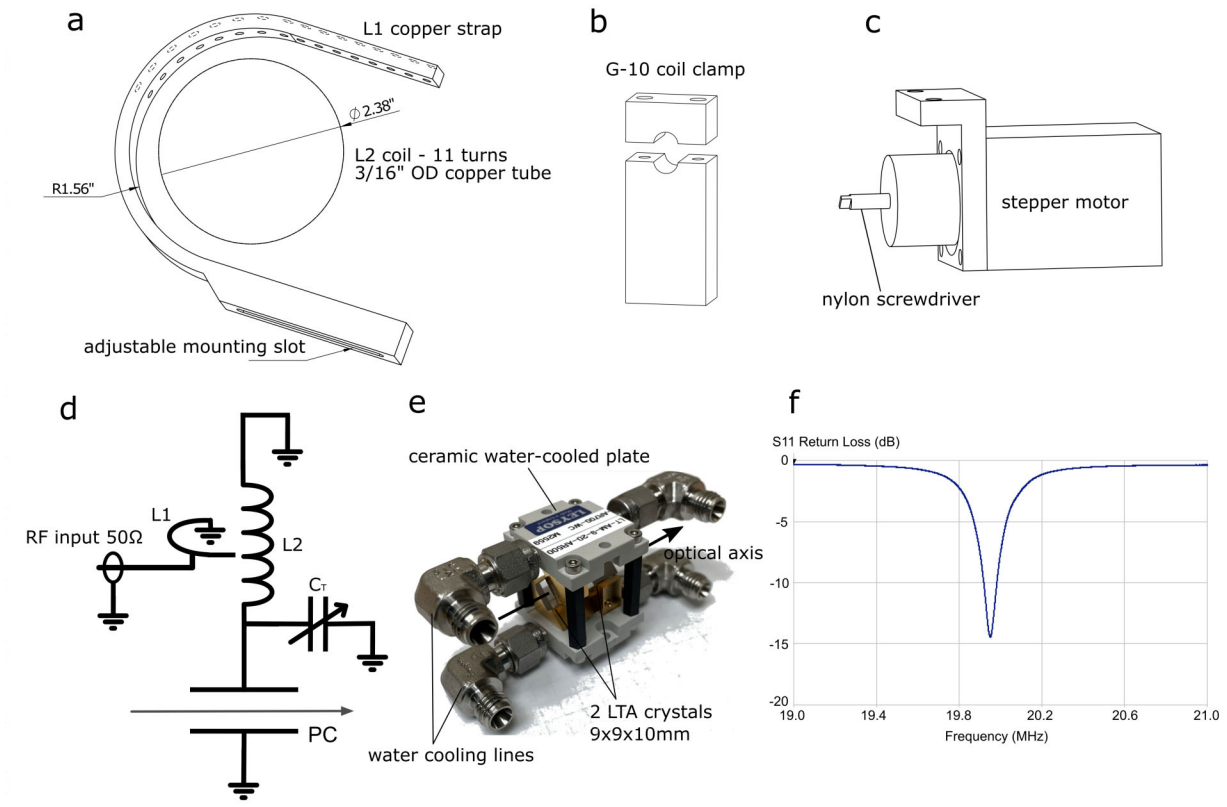

Fig. S3: System components. **(A)** Mechanical drawing of primary (L1) and secondary (L2) inductor dimensions. L2 is wound from 11 turns of 3/16" OD copper refrigeration tubing. While provisions for oil cooling were provided in the design, it was not necessary to cool L2 during operation. Adjustable tap points and mounting slot allow impedance matching to 50 Ω **(B)** Fiberglass (G-10) supports clamp the L2 coil into place **(C)** A stepper motor and screwdriver adapter allow remote tuning of a 10 pF high voltage trim capacitor C_T (Sprague-Goodman SGNMNC1103) to adjust the circuit's resonant frequency. **(D)** Electrical schematic of the resonant transformer. The primary L1 is tuned to present a 50 Ω load to the drive amplifier. **(E)** Pockels cell assembly with two lithium tantalate crystals (LTA) and optical axis indicated. The Pockels cell electrodes are water cooled through thermally conductive but electrically insulating aluminum nitride ceramic plates. **(F)** Plot of S11 return loss for the resonant transformer. An unloaded Q factor of 117 is measured which is significantly reduced under RF drive. With 9.3W input (31 V into 50 Ω) a ∼1.2 kV drive is achieved across the Pockels cell.

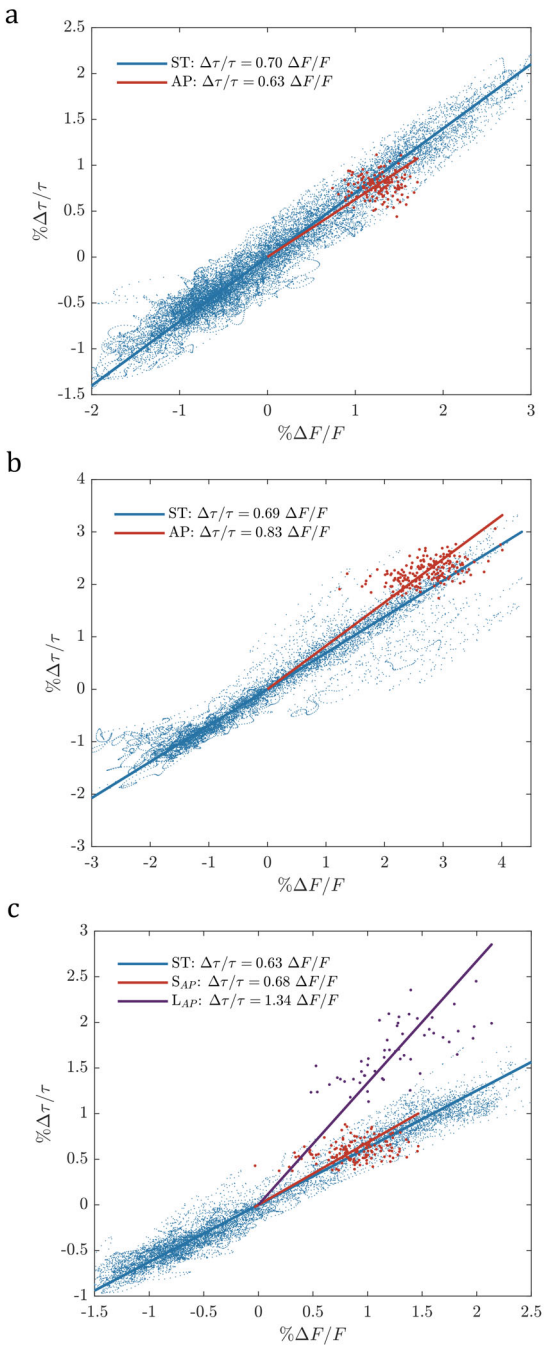

Fig. S4: Lifetime response linearity. Scatter plots of $\Delta F/F$ and $\Delta\tau/\tau$ are shown with panels A-C corresponding to the traces in Figs. 1(E), 2(A), and 2(F) respectively. Sub-threshold waveforms are plotted with a 20 Hz low-pass filter applied (blue), while action potentials are plotted separately (red) to indicate high-frequency response. Both estimates provide comparable responsivity relationships. Combined with existing calibrations for $\Delta F/F$, these plots imply a linear relationship between lifetime and membrane potential (*3, 7*). In (C), the L spikes from Fig. 2(F) are observed to have much larger lifetime responsivity than the S spikes.

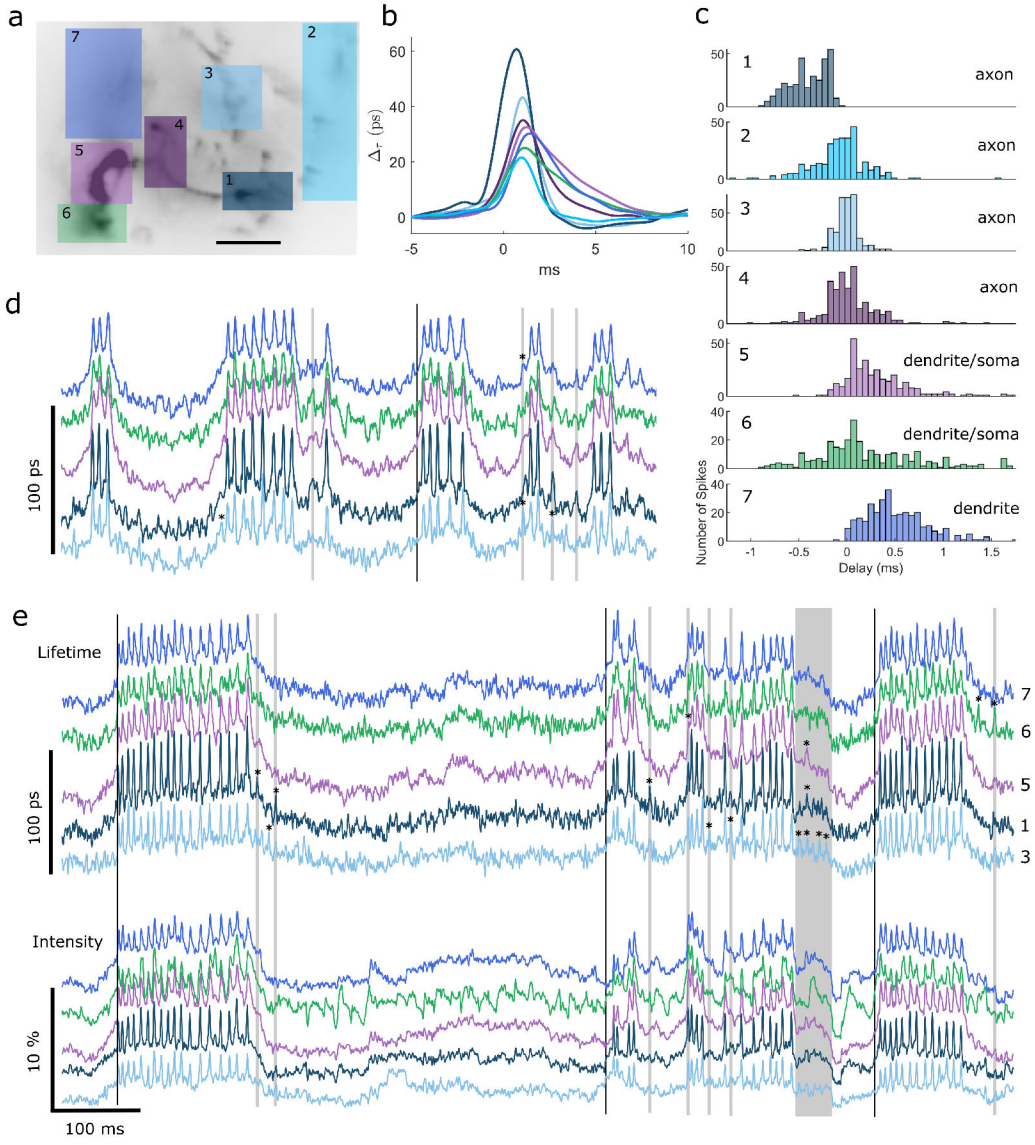

Fig. S5: Spike propagation and ROI analysis. **(A)** ROIs are defined for several labeled neuron sub-regions. **(B)** Average spike waveforms are calculated from spline-interpolated traces. **(C)** Spike delay histograms are shown. Times are calculated using the peaks of the interpolated waveform relative to the average spike time for the whole structure. Bidirectional propagation from the point of initiation is observed both to more distant axons and backwards towards dendrites and soma. **(D,E)** Comparing lifetime and intensity ROI traces (three frame moving averages) reveals stronger sub-threshold responses in the dendrites. Local effects can also be observed. Notably small spike-like depolarizations occur in the axons which do not trigger action potentials (indicated with asterisks). These depolarizations are often not resolved in the intensity trace.

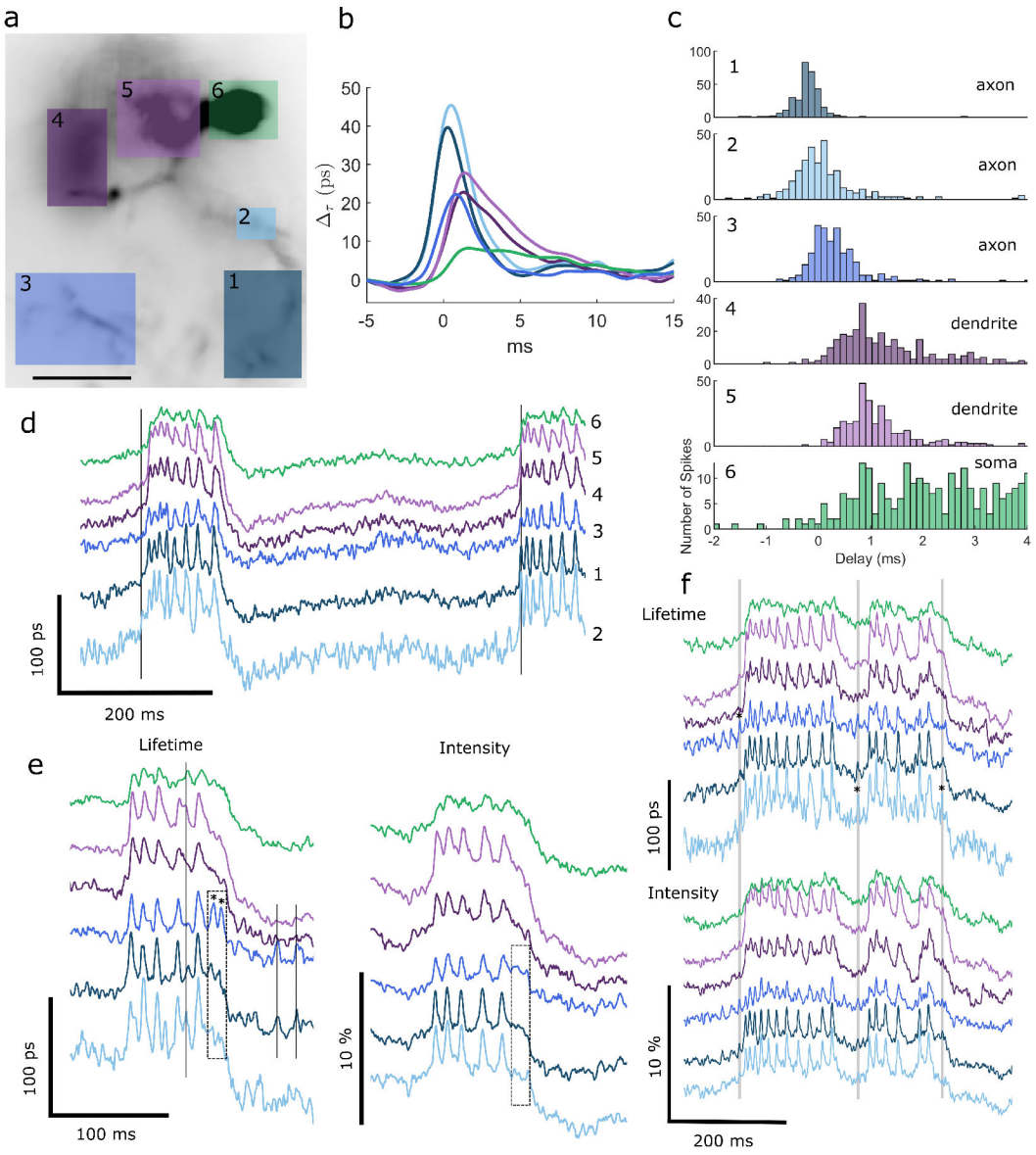

Fig. S6: Spike propagation and ROI analysis. **(A)** ROIs are defined for several labeled neuron sub-regions. **(B)** Average spike waveforms are calculated from spline-interpolated traces. **(C)** Spike delay histograms are shown. Times are calculated using the peaks of the interpolated waveform relative to the average spike time for the whole structure. Bidirectional propagation from the point of initiation is observed both to more distant axons and backwards towards dendrites and soma. **(D-F)** Comparing lifetime and intensity ROI traces (three frame moving averages) reveals stronger sub-threshold responses in the dendrites. Local effects can also be observed. Notably small spike-like depolarizations occur in the axons which do not trigger action potentials (indicated with asterisks). These depolarizations are often not resolved in the intensity trace.

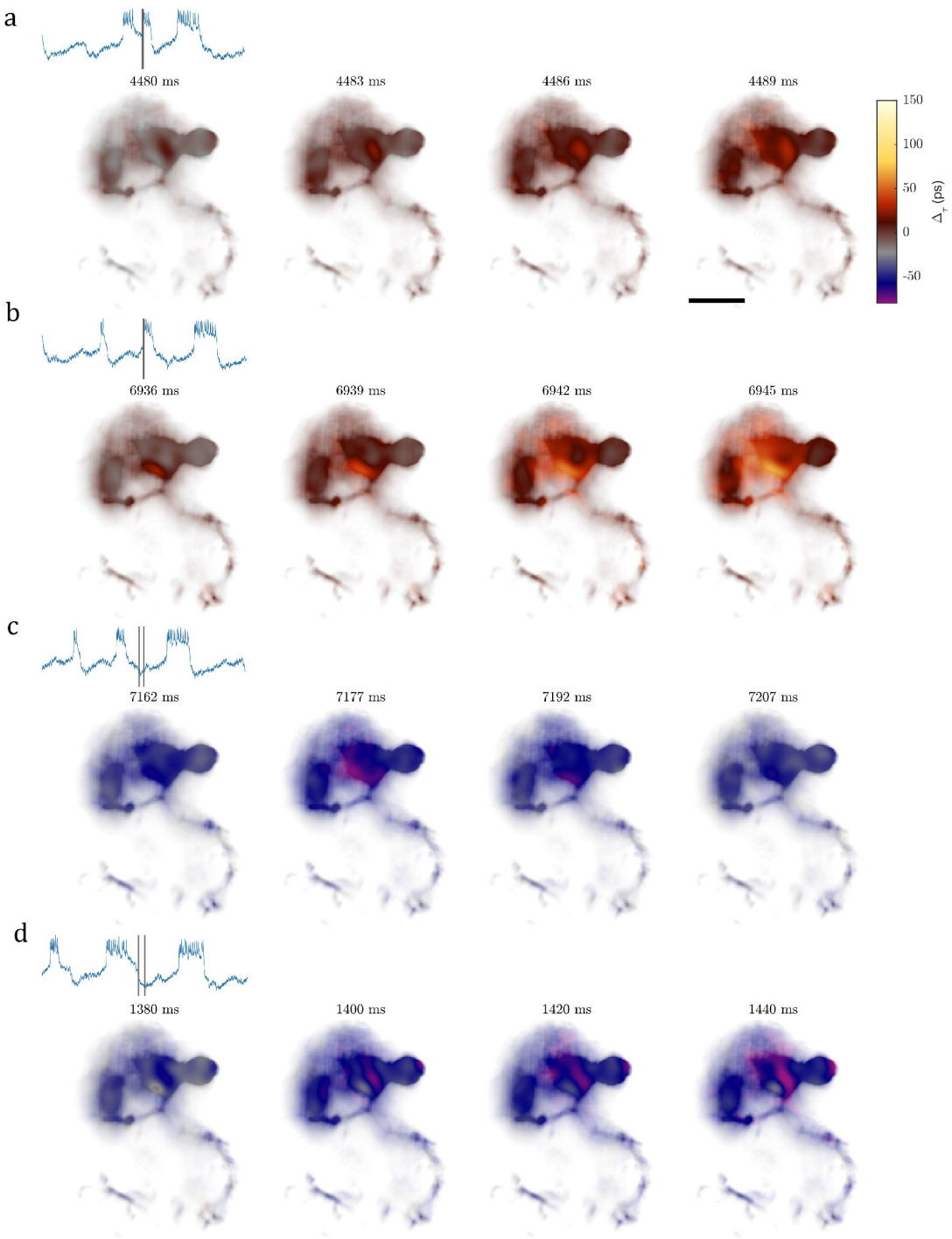

Fig. S7: Sub-threshold voltage signals localize in the dendrite. Four time-lapse image series are displayed from Movie S6 with corresponding time points indicated on the inset traces. (**A**,**B**) Some positive-going transitions appear to originate in localized regions of the dendrite. Negative sub-threshold features (**C**,**D**) have slower time dynamics but also show increased strength in the dendrite (see also Fig. S6 and Movies S6 and S7). In Movie S6 a 10 frame moving average was applied to the raw image data (scalebar 25 μm).

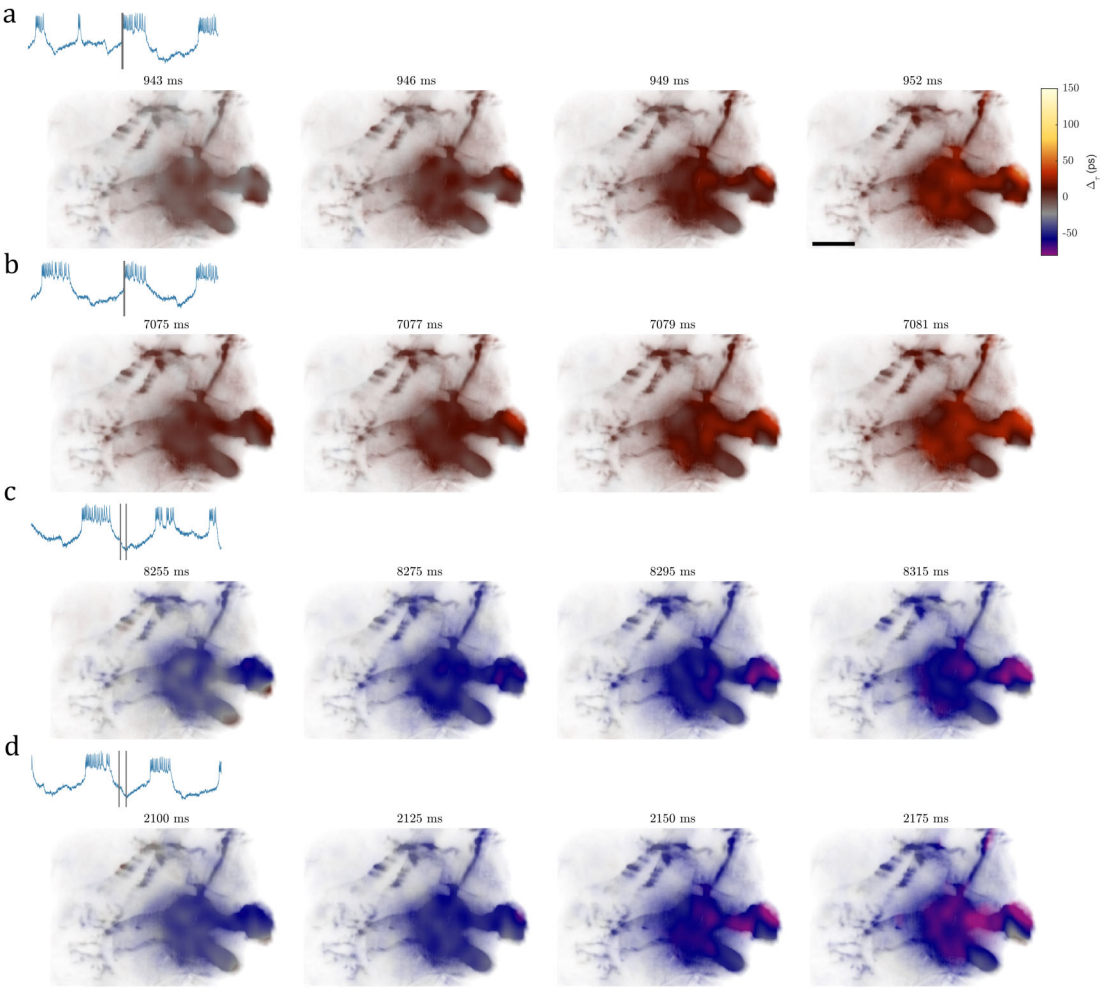

Fig. S8: Sub-threshold voltage signals localize in the dendrite. Four time-lapse image series are displayed from Movie S7 with corresponding time points indicated on the inset traces. Positive (**A**,**B**) and negative (**C**,**D**) sub-threshold voltage changes show increased strength in the dendrite. In Movie S7 a 10 frame moving average was applied to the raw image data (scalebar 25 μm).

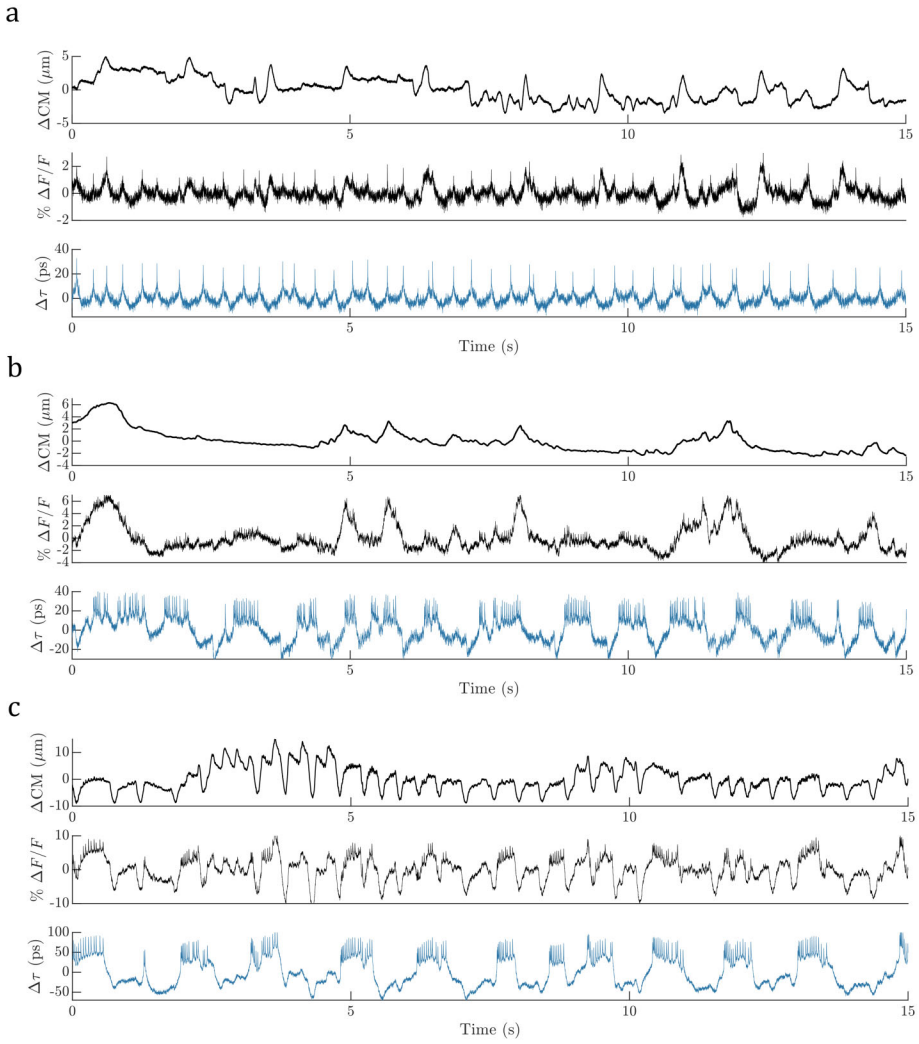

Fig. S9: Motion artifacts. Center of mass motion traces and lifetime and intensity traces are given in (A-C) for the data presented in Fig. 2(C-E). Areas with intensity artifacts strongly correlate with sample motion. Motion in the Z plane is only partially captured here.

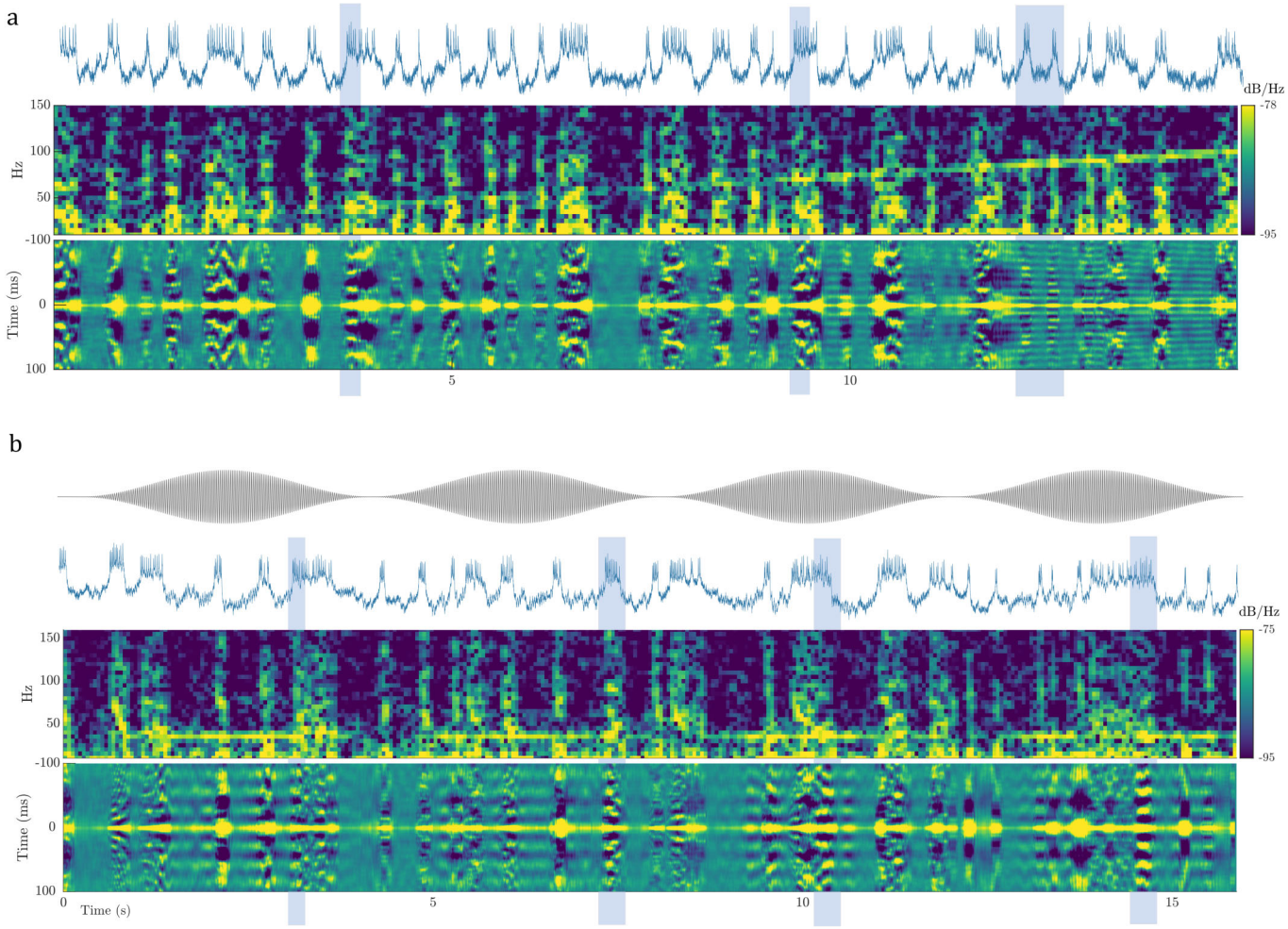

Fig. S10: Two additional examples of mechanically evoked phase locking. (**A**) Direct XY shaking stimulus ramp similar to Fig. 4. (**B**) An example using audio stimulation with periodic envelope drive (waveform displayed at top). We note that the start and stop of mechanical stimulus is usually correlated with a spike activity burst. A few example regions with phase locking are highlighted with shaded boxes. Some spike bursts demonstrate transitions between unlocked and locked behavior.

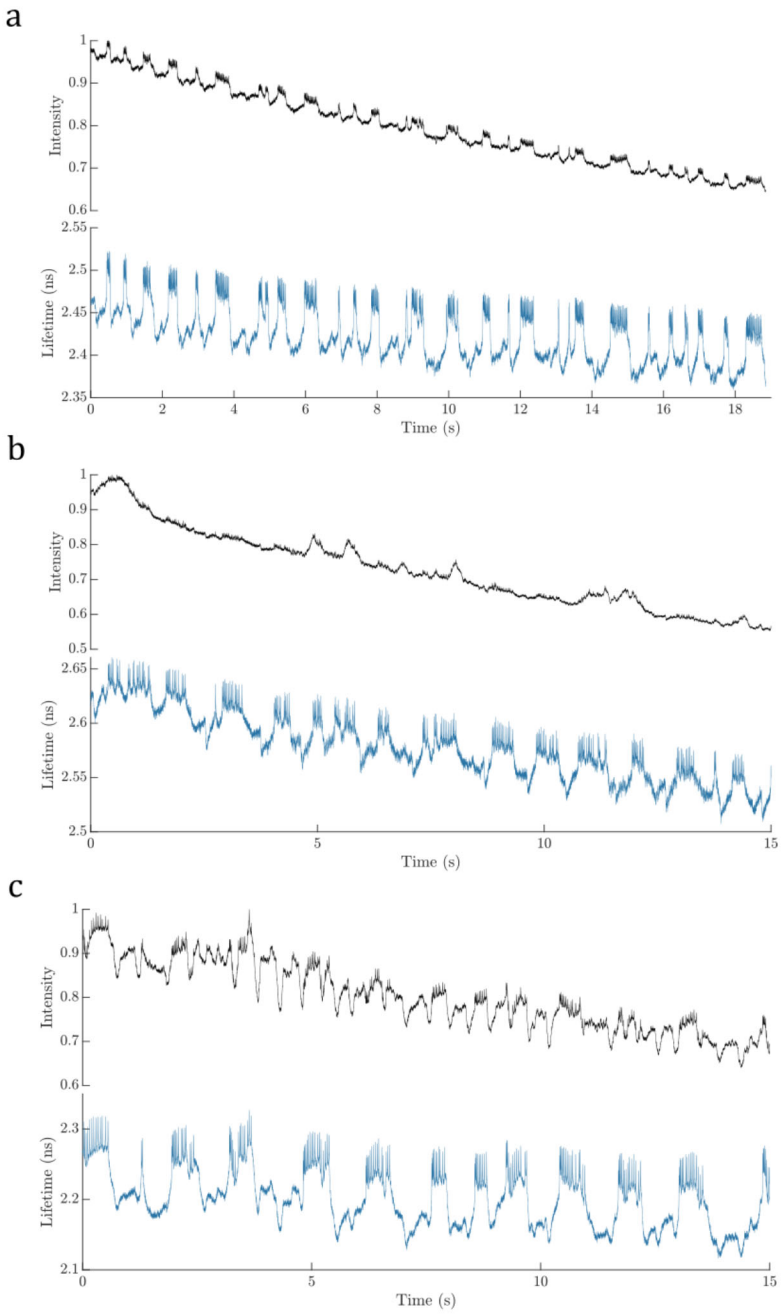

Fig. S11: Unprocessed intensity and lifetime traces show that the effects of photobleaching on GEVI intensity readout (up to 30% during a recording) are strongly suppressed by lifetime readout. Due to the presence of non-specific background fluorescence with different bleaching rate, however, there are small lifetime offsets from sample to sample and slow drifts in lifetime at the 50-100 ps level. Here plots A,B, and C correspond to the data in Figs. 1(E), 2(D), and 2(E) respectively.

Movie S1. Spike trigger averaged movie of action potential propagation (scalebar 25 μm).

Movie S2. Spike trigger averaged movie of action potential propagation (scalebar 25 μm).

Movie S3. Spike trigger averaged movie of action potential propagation (scalebar 25 μm).

Movie S4. Non-averaged movie of action potentials (scalebar 25 μm).

Movie S5. Non-averaged movie of action potentials (scalebar 25 μm).

Movie S6. Movie of sub-threshold voltage activity (10 frame moving average applied, scalebar 25 μm).

Movie S7. Movie of sub-threshold voltage activity (10 frame moving average applied, scalebar 25 μm).

Movie S8. Spike trigger averaged movie of small spikes from Fig. 2(F-L) (scalebar 25 μm).

Movie S9. Spike trigger averaged movie of large spikes from Fig. 2(F-L) (scalebar 25 μm).